

See discussions, stats, and author profiles for this publication at: <https://www.researchgate.net/publication/353607620>

Control of Travelling Crossflow Vortices Using Volume Forcing

Chapter · January 2022

DOI: 10.1007/978-3-030-67902-6_26

CITATIONS

0

READS

32

3 authors:



Zhengfei Guo

Universität Stuttgart

7 PUBLICATIONS 16 CITATIONS

SEE PROFILE



Philipp C. Dörr

Universität Stuttgart

13 PUBLICATIONS 192 CITATIONS

SEE PROFILE



Markus J. Kloker

Universität Stuttgart

173 PUBLICATIONS 2,254 CITATIONS

SEE PROFILE

Some of the authors of this publication are also working on these related projects:



DNS of compressible turbulent boundary layers [View project](#)



3D-boundary-layer transition: HLFC, Control by suction or blowing [View project](#)

Control of Travelling Crossflow Vortices using Volume Forcing

Zhengfei Guo, Philipp C. Dörr, and Markus J. Kloker

Abstract In the present DNS work we focus on the most unstable travelling crossflow vortex (CFV) mode in a 3-d boundary layer, and examine the applicability of unsteady volume-force actuation to directly tackle the invoked nonlinear state. The actuators with forcing nearly in or against the crossflow direction are arranged in a spanwise row and operated with the same frequency as that of the oncoming mode. The unsteady volume forcing can be considered as a model for actuation by plasma actuators. It is shown that unsteady forcing with a suitable phase can efficiently counteract the vortical motion of the nonlinear travelling CFVs, and hence delay the onset of secondary instabilities. However, a detrimental steady mode is also excited. The superposition of the steady and travelling modes renders some parts of the mean CFVs more unstable. By employing two additional actuator rows downstream with combined steady and unsteady forcing, the growing steady and travelling modes can be further attenuated, respectively, yielding enhanced delay of the complex transition with travelling primary 3-d structures.

1 Introduction

In swept-wing-type boundary layers the crossflow (CF) instability is the dominant mechanism of the laminar-turbulent transition. At high free-stream turbulence levels or with distributed roughness elements (DREs) on the wing in free flight with its attachment-line fluctuations, travelling crossflow vortex (CFV) modes may prevail over steady modes due to their higher growth rate. The resulting travelling CFVs quickly reach the nonlinear stage, leading to explosive secondary instabilities. Whereas the mechanism of travelling CFV dominated transition is well understood

Zhengfei Guo, Philipp C. Dörr, and Markus J. Kloker
Institute for Aerodynamics and Gas Dynamics, University of Stuttgart, Pfaffenwaldring 21, D-70550
Stuttgart, Germany, e-mail: guo/kloker@iag.uni-stuttgart.de

[2, 12, 11, 7, 10], only a small number of investigations on its control has been conducted.

In the present work we focus on the nonlinear disturbance state of travelling CFVs. Unsteady volume forcing actuators are employed to directly counteract the vortical motion of the primary CFVs and, hence, delay the onset of secondary instabilities. The volume-force distribution mimics that of an alternating-current dielectric-barrier-discharge (AC DBD) plasma actuator. The base-flow setup corresponds to the newly designed swept flat plate experiment at DLR Göttingen [1]. This study supplements a previous DNS investigation on lowering the growth rate of travelling CFVs by unsteady (upstream-flow-deformation) control vortices [8].

2 Numerical Method

2.1 Basic Setup

The compressible, high-order finite-difference code NS3D is used for the simulations presented in this work, see, e.g., Ref. [4] for details. The rectangular integration domain consists of block-structured Cartesian grids, see Fig. 1. We summarize the relevant parameters for the numerical discretization in Table 1. The inflow and outflow are treated with characteristic boundary conditions to minimize disturbance reflection. In addition, sponge zones based on a volume-forcing term and a spatial compact tenth-order low-pass filter are used. At the upper boundary, the base-flow values for ρ and T are kept, and $\partial u/\partial y|_e = \partial w/\partial y|_e = 0$ is prescribed for u and w to allow additional mass flow through the free-stream boundary; v is then calculated using the continuity equation, assuming $\partial \rho/\partial y|_e = 0$. At the isothermal wall, the no-slip condition with $\partial p/\partial y|_{\text{wall}} = 0$ is employed.

To allow computation at a non-prohibitive time step, the chordwise Mach number $Ma_\infty = 0.2$ ($Ma_{\infty, \text{exp}} = 0.066$) is chosen for the simulations. The ambient conditions and the Reynolds number are kept identical to those in the underlying experiment for similarity. The chordwise reference velocity $\bar{U}_\infty = 68.87 \text{ m s}^{-1}$

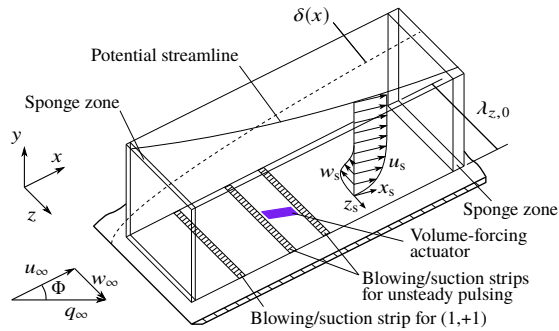


Fig. 1 Integration domain and coordinate systems.

Table 1 Numerical discretization

x explicit O8	$0.173 \leq x \leq 4.078$, 2604 equidistant points, $\Delta x = 1.5 \cdot 10^{-3}$
y explicit O8	$0.000 \leq y \leq 0.121$, 152 points with stretching, $\Delta y_{\text{wall}} = 1.251 \cdot 10^{-4}$, $\Delta y_{\text{max}}/\Delta y_{\text{wall}} = 17$
z Fourier spectral	fundamental wave number $\gamma_0 = 2\pi/\lambda_{z,0} = 70$, 10 de-aliased modes, 32 equidistant points, $\Delta z = 2.805 \cdot 10^{-3}$
t Runge-Kutta O4	fundamental angular frequency $\omega_0 = 2\pi/T_0 = 6.0$, $\Delta t = 8.727 \cdot 10^{-6}$

($\bar{U}_{\infty, \text{exp}} = 22.66 \text{ m s}^{-1}$), the reference length $\bar{L} = 0.033 \text{ m}$ ($\bar{L}_{\text{exp}} = 0.1 \text{ m}$), the reference density $\bar{\rho}_{\infty} = 1.181 \text{ kg m}^{-3}$ and the reference temperature $\bar{T}_{\infty} = \bar{T}_{\text{wall}} = 295.0 \text{ K}$ are used for normalization, with overbar denoting dimensional values. Note that \bar{L} is not the plate length $\bar{L}_{\text{plate, exp}} = 0.5 \text{ m}$. For details on the base-flow generation see Ref. [6].

Controlled disturbances are introduced at the wall using (synthetic) blowing/suction strips. At $0.766 \leq x \leq 0.835$ the integrally most amplified unsteady CFV test mode with $\gamma = 70$ is excited. This mode is denoted in the following as $(1, +1)$ in a double-spectral notation $(h\omega_0, k\gamma_0)$. To test the onset of secondary instability and initiate controlled laminar breakdown, two additional disturbance strips with a strip extension of 0.045 each are employed at $x = 2.0$ and $x = 2.5$ to excite pulse-like (background) disturbances $(h, \pm 1)$, with $h = 1 - 50$. Note that the modes $|k| \geq 2$ not directly forced by the strips are nonlinearly generated at once by the (large) primary vortex modes already present in the flow.

2.2 Localized Volume Forcing

A non-dimensional wall-parallel volume-force distribution $\hat{f}(\hat{x}, \hat{y})$ in the \hat{x} - \hat{y} -plane perpendicular to the electrode axis of a virtual plasma actuator is prescribed. The three-dimensional distribution $f(x, y, z)$ produced in a discharge area with the length l_{PA} is then modeled by extrusion of $\hat{f}(\hat{x}, \hat{y})$ along the electrode edge, as sketched in Fig. 2. At the lateral edges a 5th-order polynomial is imposed over a range of 10% electrode length to smooth the changeover from zero to maximum forcing. The angle β_{PA} defines the clockwise rotation of the electrodes about the wall-normal axis

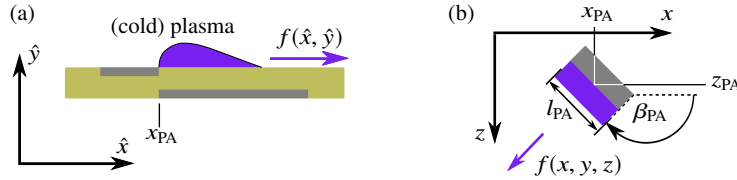


Fig. 2 (a) Plasma-actuator schematic and planar volume-force distribution. (b) Rotation about the wall-normal axis.

Table 2 Actuator parameters; f , $c_{\mu, L_{\text{exp}}}$ and c_{μ, θ_s} correspond to the time-averaged values;

$$\bar{f} = f \frac{\bar{\rho}_{\infty} \bar{U}_{\infty}^2}{L} = f \frac{\bar{\rho}_{\infty}^2 \bar{U}_{\infty}^3}{Re \bar{\mu}_{\infty}}, \max\{|\bar{f}|\} = \max\{[\bar{f}_x^2 + \bar{f}_z^2]^{1/2}\}.$$

Actuator	x_{PA}	l_{PA}	z_{PA}	β_{PA}	$\max\{ \bar{f} \}$	$c_{\mu, L_{\text{exp}}}$	c_{μ, θ_s}	c_s	c_u	ϕ_{PA}
Row 1	2.25	0.60	0.025	130.2	0.38 kN m ⁻³	5.1·10 ⁻⁶	2.2·10 ⁻³	1	6.67	7π/4
Row 2	2.75	0.25	0.070	130.2	0.38 kN m ⁻³	5.1·10 ⁻⁶	2.0·10 ⁻³	1	6.67	π/4
Row 3	3.40	0.25	0.025	133.0	3.39 kN m ⁻³	4.5·10 ⁻⁵	1.6·10 ⁻²	1	0	-

through $(x_{\text{PA}}, z_{\text{PA}})$. According to previous investigations by Dörr and Kloker [4], the effect of the wall-normal force component is negligible. The unsteadiness of the forcing is taken into account by a sinusoidal time signal:

$$f(x, y, z, t) = f(x, y, z)Z(t), \quad Z(t) = c_s + c_u \sin(\omega_{\text{PA}}t + \phi_{\text{PA}}). \quad (1)$$

With $c_s/c_u = 0.15$, the oscillating volume force with a non-zero (temporal) mean mimics the asymmetric push and pull events of the plasma actuation with low frequency, resembling the direct-frequency mode for active wave cancellation investigated by Kurz et al. [9]. To provide additional information on the forcing strength, the actuation momentum coefficient $c_{\mu, \bar{L}_{\text{exp}}}$ based on the reference length \bar{L}_{exp} is calculated using equations (3) and (4) in Dörr and Kloker [5]; c_{μ, θ_s} based on the local momentum thickness $\bar{\theta}_s$ in the streamline-oriented system is calculated as $c_{\mu, \theta_s} = c_{\mu, L_{\text{exp}}} \bar{L}_{\text{exp}}/\theta_s$. The actuator parameters for the simulations presented in this paper are summarized in Table 2.

3 Base-Flow Characteristics and Reference Case

The simulations presented in this paper refer to the redesigned swept flat-plate experiment of DLR-Göttingen [1]. The flow is strongly accelerated in the leading edge region, followed by a weak but continuous acceleration over the whole plate length. An overview of the boundary-layer parameters is given by Dörr and Kloker [6]. The stability diagram for the travelling modes with $\omega = 6$ are shown in Fig. 3(a). The investigated mode (1, +1) with $\omega = 6$ and $\gamma = 70$ is one of the integrally most amplified travelling modes. We note that the wave vector of the most amplified steady CFV mode (0, 1) is nearly perpendicular to the local potential streamlines, see e.g. Dörr and Kloker [6]. For the traveling mode (1, +1), the wave-vector angle ϕ_{α} , spanned by the x -axis and the wave vector $(\alpha_r, 0, \gamma)^T$, is about 5° smaller than that of the steady counterpart (0, 1).

In the reference case REF without control, only the test mode (1, +1) and background pulsing are activated. In Fig. 3(b), the modal amplitude development of the normalized disturbance velocity component \tilde{u}'_s is shown. It is calculated as $\tilde{u}'_s = u'_s/u_{s,e,\text{baseflow}} = (u_s - u_{s,\text{baseflow}})/u_{s,e,\text{baseflow}}$, where the subscripts s and e denote the value in the streamline-oriented system and at the boundary-layer edge,

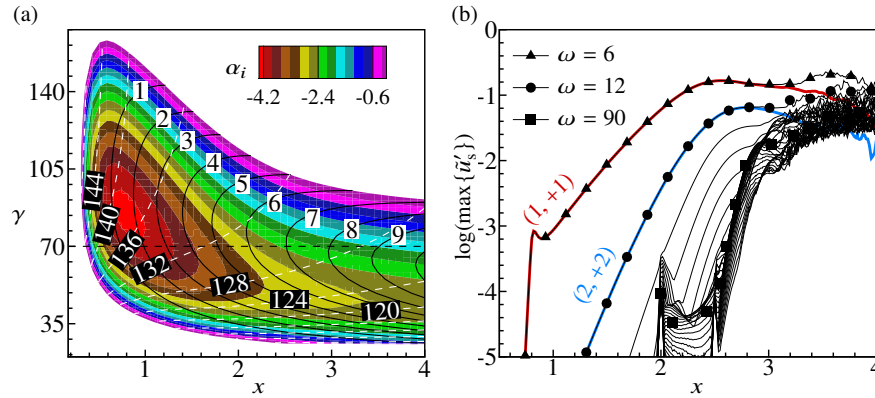


Fig. 3 (a) Spatial amplification rate $-\alpha_i$ (colour), n -factor (solid lines) and wave-vector angle ϕ_α (white dashed lines) of unstable CFV modes with $\omega = 6$. (b) Downstream development of modal disturbance amplitudes $\tilde{u}'_{s,(h,k)}$ and $\tilde{u}'_{s,(h)}$ (maximum over y or y and z , $6 \leq \omega \leq 180$, $\Delta\omega = 6$) for case REF.

respectively. The amplitude of the test mode (1, +1) rises continuously to 10% at $x \approx 2.2$. The superharmonics ($k, +k$), $k \geq 2$, are nonlinearly generated and saturate progressively with the generating mode (1, +1). At $x \approx 2.5$, an explosive secondary instability is triggered. The high-frequency mode $\omega = 90$ is the most strongly amplified secondary mode, and laminar breakdown sets in slightly downstream.

In Figs. 4(a)-(d), snapshots of the vortical structures at four time instances within a fundamental period T_0 are presented. The co-rotating CFVs appearing in the visualized region travel in the positive z -direction while convecting downstream. The orientation of the vortex axis is perpendicular to the wave-vector of the mode

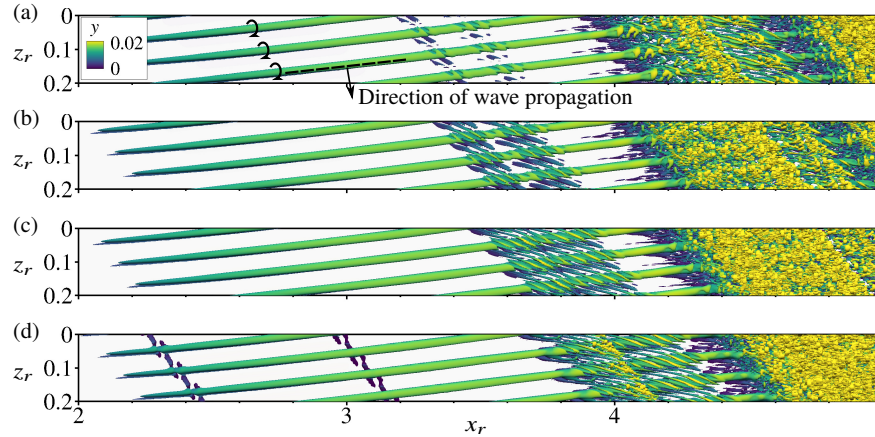


Fig. 4 Vortex visualization (snapshots, $\lambda_2 = -4$) for case REF at $t/T_0 = 13.25$ (a), 13.5 (b), 13.75 (c), 13 (e). Rotated reference system used. Not to scale.

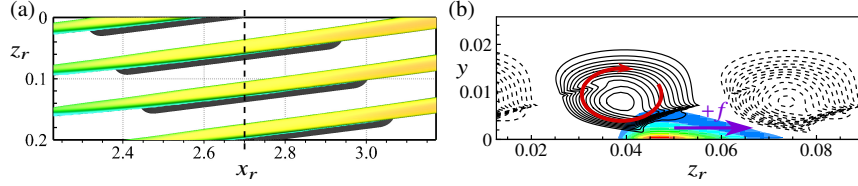


Fig. 5 (a) Travelling CFVs to be controlled ($\lambda = -4$, coloured) and volume-force distribution ($f_{10\%}$ -isosurface, black) for case DA-1. Rotated reference system used. (b) Crosscut along the dashed line in (a). Colour indicates $|f|$ (levels 0.05 to 0.75, $\Delta = 0.10$). Solid and dashed lines show λ_2 -isocontours (levels -12 to -1 , $\Delta = 1$) of the travelling CFVs at the time of maximum positive and negative forcing, respectively.

(1, +1), therefore misaligned with the local potential streamlines. The finger-like structures emerging on the main CFVs correspond to the secondarily amplified high-frequency modes, finally developing into turbulence spots.

4 Investigations of Control

4.1 Single Row of Actuators

A spanwise row of volume-forcing actuators as described in Sect. 2.2 is now employed to control the transition induced by travelling CFVs. In Fig. 5, the (inactive) volume-forcing setup is shown in a top view and a crosscut. The spanwise spacing of the actuators corresponds to the spanwise wavelength of the targeted travelling mode (1, +1). To ensure an effective wave cancellation, the actuators are aligned with the wave crests of (1, +1). The induced unsteady volume force is then perpendicular to the axes of the oncoming CFVs, aimed at counteracting the rotational motion in the near wall region. The forcing towards the wave-vector direction is defined as positive. The spanwise position of the localized forcing is arbitrarily chosen while the forcing strength $\max|f|$ and the phase of the time signal $Z(t)$ are varied until the most delayed transition is found.

For the most effectively controlled case DA-1, the volume force attains its (positive) maximum at $t = 0.375T_0$. The vortical structures arising from the actuation during one fundamental period are shown in Fig. 6. The oncoming CFVs are clearly affected while travelling over the actuators. Farther downstream, their strength is decreased and their shape is strongly modulated in streamwise direction. Thanks to the attenuation of the primary vortices, the first secondary structures appear only at $x_r > 4.0$, and the transition is delayed compared to the reference case.

In Fig. 7(a), the downstream development of modal disturbance amplitudes for case DA-1 is shown. As expected, the oncoming CFV mode (1, +1) is clearly attenuated in the vicinity of the actuators. Consequently, the onset of the secondary growth of high-frequency modes is delayed from $x \approx 2.5$ to $x \approx 3.0$. It is noteworthy

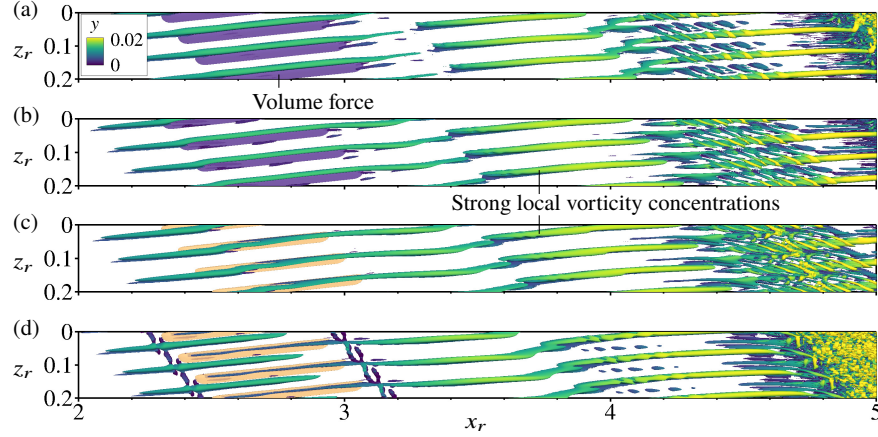


Fig. 6 Vortex visualization (snapshots, $\lambda_2 = -4$) and volume-force distribution ($f_{i0\%}$ -isosurface, purple: positive; orange: negative) for case DA-1 at $t/T_0 = 13.25$ (a), 13.5 (b), 13.75 (c), 13 (d). Rotated reference system used. Not to scale.

that a steady mode $(0, 1)$ is also excited by the volume forcing due to the non-zero steady mean. This mode undergoes a continuous amplification farther downstream, and attains a nonlinear amplitude comparable with the travelling mode $(1, +1)$. The streamwise modulation of the main CFVs in the physical space can be explained as a result of the superposition of the modes $(0, 1)$ and $(1, +1)$. The constructive interference between both misaligned modes leads to emergence of some travelling 3-d structures associated with strong local vorticity concentrations, where the secondary finger-structures first appear. It is justified to say that the modes $(1, +1)$ and $(0, 1)$ are jointly responsible for the final breakdown. See [3] for a more detailed discussion on the laminar breakdown initiated by superposed steady and travelling modes.

To minimize the detrimental effect of the actuation induced steady mode $(0, 1)$, an additional simulation with purely sinusoidal forcing, i.e. $c_s = 0$, is performed. As shown by the dashed line in Fig. 7(a), the amplitude of $(0, 1)$ is indeed reduced in the vicinity of the actuator row. However, it grows to the same level as in case DA-1 farther downstream, and the control performance is virtually the same. We note that, the unsteady force component excites the modal spectral contents $(1, \pm k)$ simultaneously. Even when the steady force component is absent, the steady mode $(0, 1)$ can still be generated by nonlinear interaction between travelling modes, e.g. by $(1, +1)$ and $(1, +2)$.

Preliminary investigations have shown that employing shorter actuators leads to a higher initial amplitude of the unwanted steady mode $(0, 1)$. Transition delay is only achievable by using actuators with a sufficient length l_{PA} . In fact, the actuators favour only wave structures aligned with their spatial arrangement, i.e. the misaligned steady mode $(0, 1)$ is hindered. Extending the actuator's length along the wave crests of the target mode helps intensify this receptivity selection effect.

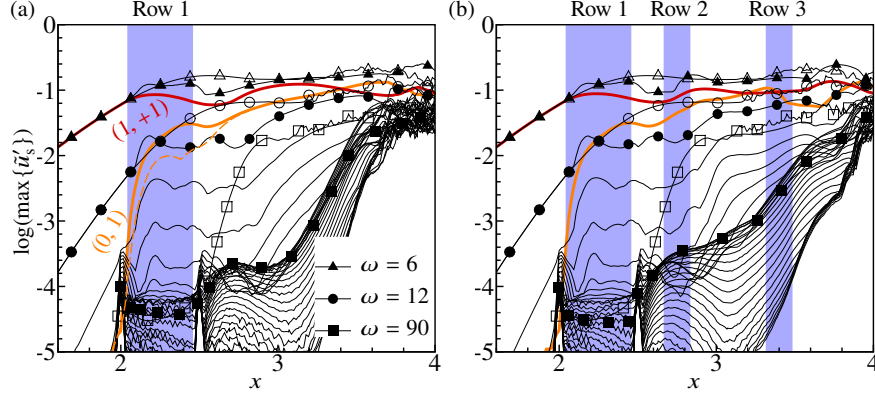


Fig. 7 Downstream development of modal disturbance amplitudes $\bar{u}'_{s,(h,k)}$ and $\bar{u}'_{s,(h)}$ (maximum over y or y and z , $6 \leq \omega \leq 180$, $\Delta\omega = 6$) for case (a) DA-1 and (b) DA-3. The dashed line in (a) shows the mode (0,1) for case DA-1- $(c_s = 0)$. Open symbols denote the reference case REF. Blue rectangles mark the locations of volume forcing.

4.2 Multiple Rows of Actuators

We now add two additional actuator rows downstream to attenuate the remaining CFVs for improvement of the transition delay. The second and third row are aimed at breaking the downstream growth of the mode (1, +1) and (0, 1), respectively. Since the main CFVs downstream of the first actuator row are strongly deformed, it is not possible to use elongated actuators along the CFVs. Instead, shorter actuators with more localized forcing are employed. The second row is centered at $x = 2.75$, before the travelling mode (1, +1) attains an amplitude of 10%. The orientation and the time signal of the actuators are identical to those used for the first row. The spanwise location and the phase of the time signal is adapted to delay the transition as far as possible. For the third row, steady forcing is employed at $x = 3.4$ to kill the steady CFV mode dominating farther downstream. The actuators are aligned with the orientation of the steady mode (0, 1). Note that this strategy is based on knowledge of previous [5] and the current investigations, and on educated intuition; prospectively the use of a controller would secure the control efficiency at varied conditions.

As shown in Fig. 7(b), the modes (1, +1) and (0, 1) are locally attenuated by the second and third actuator row, respectively. However, it seems that weakening one of both modes promotes the downstream growth of the other. The secondary growth of the high-frequency modes is only slightly slowed down. Vortex visualization in Fig. 8 shows that the strength of the main CFVs is further reduced by the additional actuator rows. The first turbulence spots appear only at the end of the visualized region. It also makes clear that a perfect wave cancellation using localized forcing is hardly attainable in such a complex scenario. A rigorous, in-situ optimization of the forcing configuration is necessary in practice.

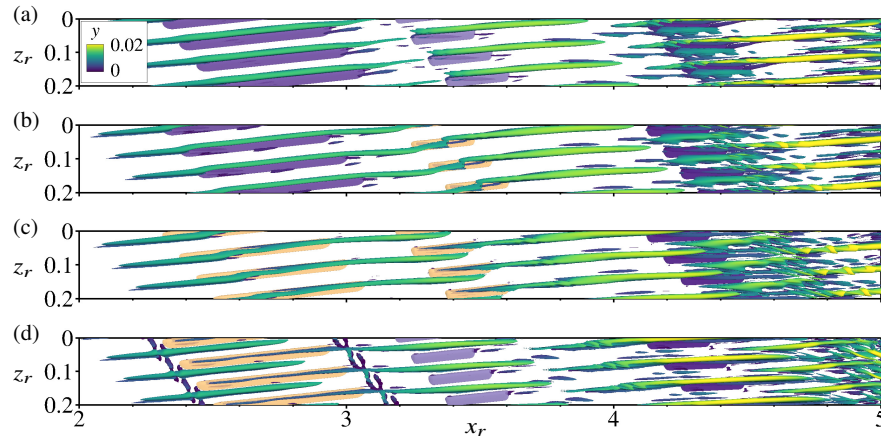
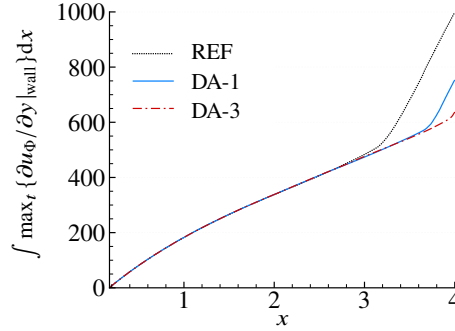


Fig. 8 Vortex visualization (snapshots, $\lambda_2 = -4$) and volume-force distribution ($f_{10\%}$ -isosurface, purple: positive; orange: negative) for case DA-3 at $t/T_0 = 13.25$ (a), 13.5 (b), 13.75 (c), 13 (e). Rotated reference system used. Not to scale.

Fig. 9 In the x -direction integrated wall-normal gradient of the spanwise mean velocity u_Φ . The maximum arising over one fundamental period is used to account for a fully turbulent flow.



The effect of the wave attenuation on the skin-friction drag is compared in Fig. 9. The spanwise averaged wall-normal gradient $\partial u_\Phi / \partial y$ is integrated in the x -direction to indicate the skin-friction development, where u_Φ is the velocity component in the direction of the oncoming flow. The sudden slope change of the curves implies the location of the transition front. It is shown that the total skin-friction drag is successively reduced by three actuator rows due to the delayed transition.

5 Conclusions

The applicability of volume-forcing actuators to control large-amplitude travelling crossflow vortices has been explored. The localized, unsteady volume force mimics the effect of plasma actuators operated at low-frequency. The unsteady forcing (with alternating direction) is aimed at counteracting the rotational motion of the travelling

CFVs in the nonlinear state. The actuators are arranged in a spanwise row and oriented parallel to the wave crests of the oncoming travelling CFVs. It is shown that the onset of secondary instabilities can be delayed by attenuating the primary vortices using unsteady volume forcing. However, it is found that a detrimental steady mode is also excited. It grows in amplitude and modulates the primary vortical structures, leading to an emergence of isolated structures associated with strong local vorticity concentrations, rendering some parts of the main CFVs more unstable. By employing two additional actuator rows downstream with combined steady and unsteady forcing, the growing steady and travelling modes can be further attenuated, respectively, yielding enhanced delay of the complex transition scenario with travelling primary 3-d structures. Therefore it is proven that a control is principally feasible. However a controller is needed if the travelling vortices to be controlled do not come as regular as investigated here.

References

1. Barth, H., Hein, S., Rosemann, H.: Redesigned swept flat-plate experiment for crossflow-induced transition studies. In: *New Results in Numerical and Experimental Fluid Dynamics XI, Notes on Numerical Fluid Mechanics and Multidisciplinary Design*. Springer Berlin (2017)
2. Bippes, H.: Basic experiments on transition in three-dimensional boundary layers dominated by crossflow instability. *Prog. Aerosp. Sci.* **35**, 363–412 (1999)
3. Bonfigli, G., Kloker, M.: Numerical investigation of transition caused by superposed steady and travelling crossflow vortices. Tech. Rep. IAG-TR-2005-CFTRANS, University of Stuttgart, Institute of Aerodynamics and Gas Dynamics (2005). DOI 10.13140/RG.2.2.25411.35366
4. Dörr, P.C., Kloker, M.J.: Stabilisation of a three-dimensional boundary layer by base-flow manipulation using plasma actuators. *J. Phys. D: Appl. Phys.* **48**, 285205 (2015)
5. Dörr, P.C., Kloker, M.J.: Transition control in a three-dimensional boundary layer by direct attenuation of nonlinear crossflow vortices using plasma actuators. *Int. J. Heat Fluid Flow* **61**, 449–465 (2016)
6. Dörr, P.C., Kloker, M.J.: Crossflow transition control by upstream flow deformation using plasma actuators. *J. Appl. Phys.* **121**, 063303 (2017)
7. Downs, R.S., White, E.B.: Free-stream turbulence and the development of cross-flow disturbances. *J. Fluid Mech.* **735**, 347–380 (2013)
8. Guo, Z., Kloker, M.J.: Control of crossflow-vortex-induced transition by unsteady control vortices. *Journal of Fluid Mechanics* **871**, 427–449 (2019)
9. Kurz, A., Tropea, C., Grundmann, S., Forte, M., Vermeersch, O., Seraudie, A., Arnal, D., Goldin, N., King, R.: Transition delay using DBD plasma actuators in direct frequency mode. *AIAA Paper* (2012). 2012-2945
10. Li, F., Choudhari, M.M., Duan, L., Chang, C.L.: Nonlinear development and secondary instability of traveling crossflow vortices. *Phys. Fluids* **26**, 064104 (2014)
11. Saric, W.S., Reed, H.L., White, E.B.: Stability and transition of three-dimensional boundary layers. *Ann. Rev. Fluid Mech.* **35**, 413–440 (2003)
12. Wassermann, P., Kloker, M.: Transition mechanisms induced by travelling crossflow vortices in a three-dimensional boundary layer. *J. Fluid Mech.* **483**, 67–89 (2003)